APPLIED SCIENCES AND ENGINEERING

Fully 3D-printed soft robots with integrated fluidic circuitry

Joshua D. Hubbard[1,2,3†], Ruben Acevedo[2,3†], Kristen M. Edwards[2,3,4], Abdullah T. Alsharhan[2‡], Ziteng Wen[2,3], Jennifer Landry[2,3], Kejin Wang[2], Saul Schaffer[2,3,5], Ryan D. Sochol[2,3,6,7*]

The emergence of soft robots has presented new challenges associated with controlling the underlying fluidics of such systems. Here, we introduce a strategy for additively manufacturing unified soft robots comprising fully integrated fluidic circuitry in a single print run via PolyJet three-dimensional (3D) printing. We explore the efficacy of this approach for soft robots designed to leverage novel 3D fluidic circuit elements—e.g., fluidic diodes, "normally closed" transistors, and "normally open" transistors with geometrically tunable pressure-gain functionalities—to operate in response to fluidic analogs of conventional electronic signals, including constant-flow ["direct current (DC)"], "alternating current (AC)"–inspired, and preprogrammed aperiodic ("variable current") input conditions. By enabling fully integrated soft robotic entities (composed of soft actuators, fluidic circuitry, and body features) to be rapidly disseminated, modified on demand, and 3D-printed in a single run, the presented design and additive manufacturing strategy offers unique promise to catalyze new classes of soft robots.

INTRODUCTION

Over the past decade, the field of soft robotics has established itself as distinctively suited for applications that would be difficult or impossible to realize using traditional, rigid robots (*1*–*3*). The reliance on compliant materials that are actuated by fluidic means (e.g., hydraulics and/or pneumatics) facilitates a number of inherent benefits for soft robots, particularly in terms of safety for human-robot interactions, lower costs, and adaptability in geometry for manipulating complex and/or delicate objects (*4*–*6*). At present, however, a critical barrier to the utility of soft robots stems from the requirement that increasing the number of independently operated soft actuators (or degrees of freedom) typically demands an equal or greater number of distinct control inputs (*7*–*9*). To reduce or obviate the need for such external control schemes, researchers have investigated a wide range of approaches for enhancing soft robot autonomy via fluidic logic (*10*–*12*).

In contrast to efforts in which independent fluidic circuitry is manually connected to soft robots (*13*, *14*), there is growing interest in the ability to embed such functions directly inside of soft robotic systems (*15*). Of particular note is a hybrid strategy reported by Wehner *et al.*, which entailed using clean room–based multilayer soft lithography protocols to fabricate a microfluidic oscillator (*16*) and then harnessing a variety of manufacturing techniques—e.g., computer numerical control machining, multimaterial casting, embedded sacrificial direct ink writing, thermal curing/evacuation processes, and laser cutting—to ultimately achieve an untethered soft "octobot" capable of periodic actuations (*17*). Since its introduction, however, this manufacturing methodology has yet to find broad adoption in the soft robotics community (*18*), possibly due to the reliance on soft lithography–based fluidic circuits. Specifically, the use of multilayer soft lithography approaches for integrated fluidic circuit fabrication presents a number of challenges, including those associated with: (i) cost, time, and/or labor requirements for executing microfabrication protocols; (ii) access and training restrictions (e.g., to use clean room facilities and equipment); (iii) variability in device efficacy and/or reproducibility due to user skill–based manual alignment steps; and (iv) geometric (i.e., planar or "2.5D") limitations inherent to photolithography and micromolding processes (*19*). Furthermore, while researchers have demonstrated a wide range of fluidic valving capabilities (*16*, *20*–*22*), enabling more sophisticated functionalities—particularly those based on pressure-gain operations—is not straightforward based on such fabrication methodologies (*23*, *24*).

To bypass the aforementioned challenges at larger scales, Rothemund *et al.* introduced soft, bistable valves that serve as fluidic analogs to electronic Schmitt triggers (*24*). Researchers have integrated these valves with soft actuators to yield gripping, undulating, and rolling operations for soft robotic systems (*24*–*26*). Recently, Drotman *et al.* further extended the use of these valves to control the gait of an autonomous walking robot with embedded sensing operations (*27*). Despite these capabilities, one caveat is the substantial reliance on manual protocols by which the multicomponent valves and systems are assembled by hand (e.g., using glues and/or fasteners) (*24*–*27*), which can present similar challenges in terms of user skill–associated efficacy and reproducibility. Consequently, alternative approaches for manufacturing fluidic circuitry–based soft robots remain in critical demand (*28*).

Here, we present a novel strategy for additively manufacturing unified soft robotic systems with fully integrated fluidic circuitry in a single print run via multimaterial "PolyJet three-dimensional (3D) printing" (Fig. 1). Initially, modular components, such as fluidic circuit elements, interconnects, and access ports as well as soft robotic actuators and structural members (Fig. 1A), can be designed and assembled within computer-aided design (CAD) software to

[1]Department of Chemical Engineering, University of California, Berkeley, CA 94720, USA. [2]Department of Mechanical Engineering, University of Maryland, College Park, MD 20742, USA. [3]Maryland Robotics Center, University of Maryland, College Park, MD 20742, USA. [4]Department of Mechanical Engineering, Massachusetts Institute of Technology, Cambridge, MA 02139, USA. [5]Department of Mechanical Engineering, Carnegie Mellon University, Pittsburgh, PA 15213, USA. [6]Department of Bioengineering, University of Maryland, College Park, MD 20742, USA. [7]Robert E. Fischell Institute of Biomedical Devices, University of Maryland, College Park, MD 20742, USA.
*Corresponding author. Email: rsochol@umd.edu
†These authors contributed equally to this work.
‡Present address: Department of Mechanical Engineering, Kuwait University, Safat, Kuwait.

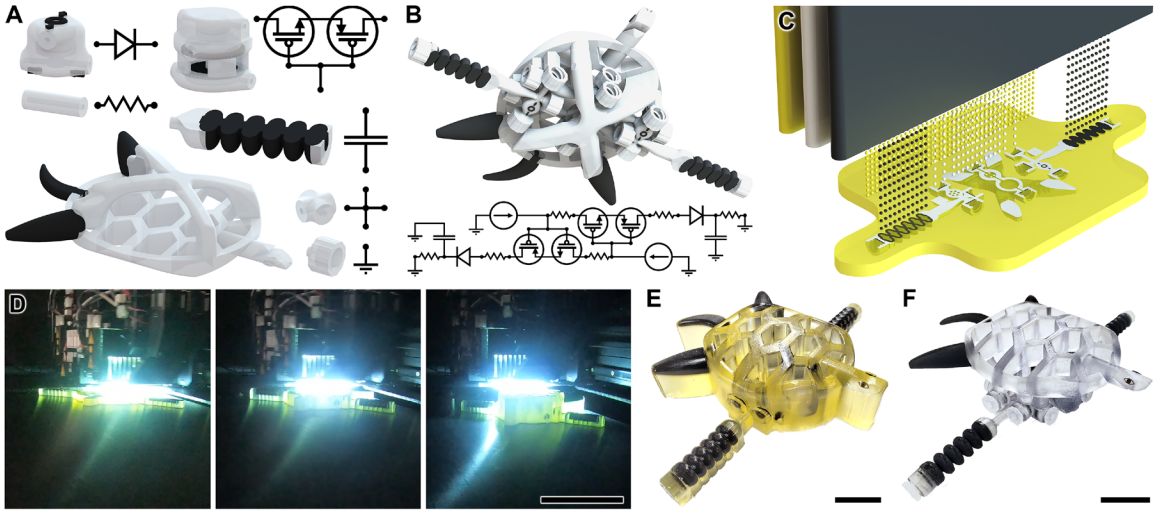

Fig. 1. Design and additive manufacturing strategy for PolyJet 3D printing unified soft robotic systems comprising fully integrated fluidic circuitry in a single print run. (**A**) Modular 3D CAD models and analogous electronic circuit symbols of fluidic circuit elements, fluidic interconnects, soft actuators, and structural casing. (**B**) CAD model and corresponding analogous circuit diagram of a unified soft robot with a fully integrated fluidic oscillator circuit. (**C**) Conceptual illustration of multimaterial PolyJet 3D printing the soft robot using compliant (black), rigid (white), and water-soluble support (yellow) materials. (**D**) Sequential time-lapse images of the PolyJet 3D printing process. Scale bar, 5 cm; see also movie S1. (**E** and **F**) Fabrication results for the unified multimaterial soft robot with integrated fluidic circuitry (E) before and (F) after support material removal. Scale bars, 2 cm. Photo credits: Ruben Acevedo, University of Maryland College Park.

generate a 3D model of a soft robot with fully integrated fluidic circuitry (Fig. 1B). Although researchers have used a wide range of additive manufacturing technologies in the fields of soft robotics (*29*–*31*) and fluidic circuitry (*32*–*36*), we propose that PolyJet 3D printing is uniquely suitable for fabricating both classes of systems simultaneously as unified entities. PolyJet printing is an inkjet-based ("material jetting") process in which multiple photoreactive and sacrificial support materials are dispensed in parallel (with continual ultraviolet dosing) to produce 3D objects in a line-by-line, layer-by-layer manner. Previously, researchers have reported the use of PolyJet printing for constructing soft actuators and robots (i.e., without fluidic circuitry) (*37*–*40*) as well as independent fluidic valves (*41*). In this work, however, we additively manufacture fully integrated soft robotic systems—i.e., including all of the soft actuators; body features (of arbitrary design); and fluidic circuit elements, interconnects, and ports—in a single print run (Fig. 1, C and D, and movie S1). This process entails the concurrent printing of three distinct materials: (i) a compliant photopolymer (Fig. 1C, black), (ii) a rigid photoplastic material (Fig. 1C, white), and (iii) a sacrificial water-soluble support material (Fig. 1C, yellow). One caveat to the use of the sacrificial support material is that it must be removed or dissolved from outer regions as well as internal voids and channels following the printing process (Fig. 1E). Researchers have demonstrated a number of techniques to minimize (*42*, *43*) and even bypass the support removal process completely (*40*, *44*); however, to promote broad accessibility, here, we use a hybrid approach that incorporates manual removal steps (e.g., on the order of tens of minutes) with autonomous dissolution protocols. In combination, the totality of the PolyJet-based additive manufacturing and postprocessing methodology—the vast majority of which being autonomous—can be executed in less than a day to realize 3D multimaterial soft robots with fully integrated fluidic circuitry (e.g., Fig. 1F).

To explore the utility of the presented strategy, first, we introduce and characterize a fundamental class of PolyJet-enabled fluidic circuit elements—namely, fluidic diodes, "normally closed" fluidic transistors, and "normally open" fluidic transistors that support facile geometric customization of their pressure-gain properties—from which sophisticated fluidic circuits can be built. We then investigate the operational performance of three soft robots with distinct integrated fluidic circuits designed with respect to fluidic analogs of conventional electrical signals, including (i) a soft robotic turtle that yields periodic, out-of-phase actuation routines for its soft limbs under constant-flow ["direct current (DC)"] input conditions; (ii) a soft robotic turtle that leverages embedded fluidic transistors with distinct pressure-gain properties to generate periodic swimming-inspired motions under sinusoidal ["alternating current (AC)"] fluidic input conditions; and (iii) a soft robotic hand capable of completing the first level of the original "Super Mario Bros." video game in real time based on a single preprogrammed aperiodic ("variable current") pressure input.

RESULTS

PolyJet 3D-printed fluidic circuit elements

The multimaterial and geometric versatility inherent to PolyJet 3D printing provides two key benefits for fluidic circuit element manufacturing. In contrast to previous single-material work from our group (*34*) and others (*32*, *33*), the incorporation of materials that differ in rigidity serves to enhance performance by allowing the material properties of specific features to be tailored to complement desired functionalities. For example, features designed to deform during operation, such as diaphragms and O-rings, can be constructed using a compliant material, while those designed to be functionally static (e.g., fluidic channels, access ports, and structural casings) can be built using a rigid material. In addition, the simultaneous deposition of a sacrificial support material allows for internal components to be printed in "free-floating" configurations (i.e., without traditional support structures or attachments of any kind). These attributes provide a unique pathway

to realize designs and functionalities for fluidic diodes (Fig. 2, A to D) and fluidic transistors (Fig. 2, E to S) that would be difficult or infeasible to achieve via alternative manufacturing methods.

The 3D fluidic diode architecture in this work includes two main components: (i) a rigid-material structural casing with internal channels that include a central region with a single top orifice and multiple bottom orifices and (ii) a free-floating sealing disc that is primarily composed of a rigid material but notably includes a compliant-material O-ring on top to support sealing via rigid-compliant material interactions (Fig. 2A). The operating principle of the fluidic diode

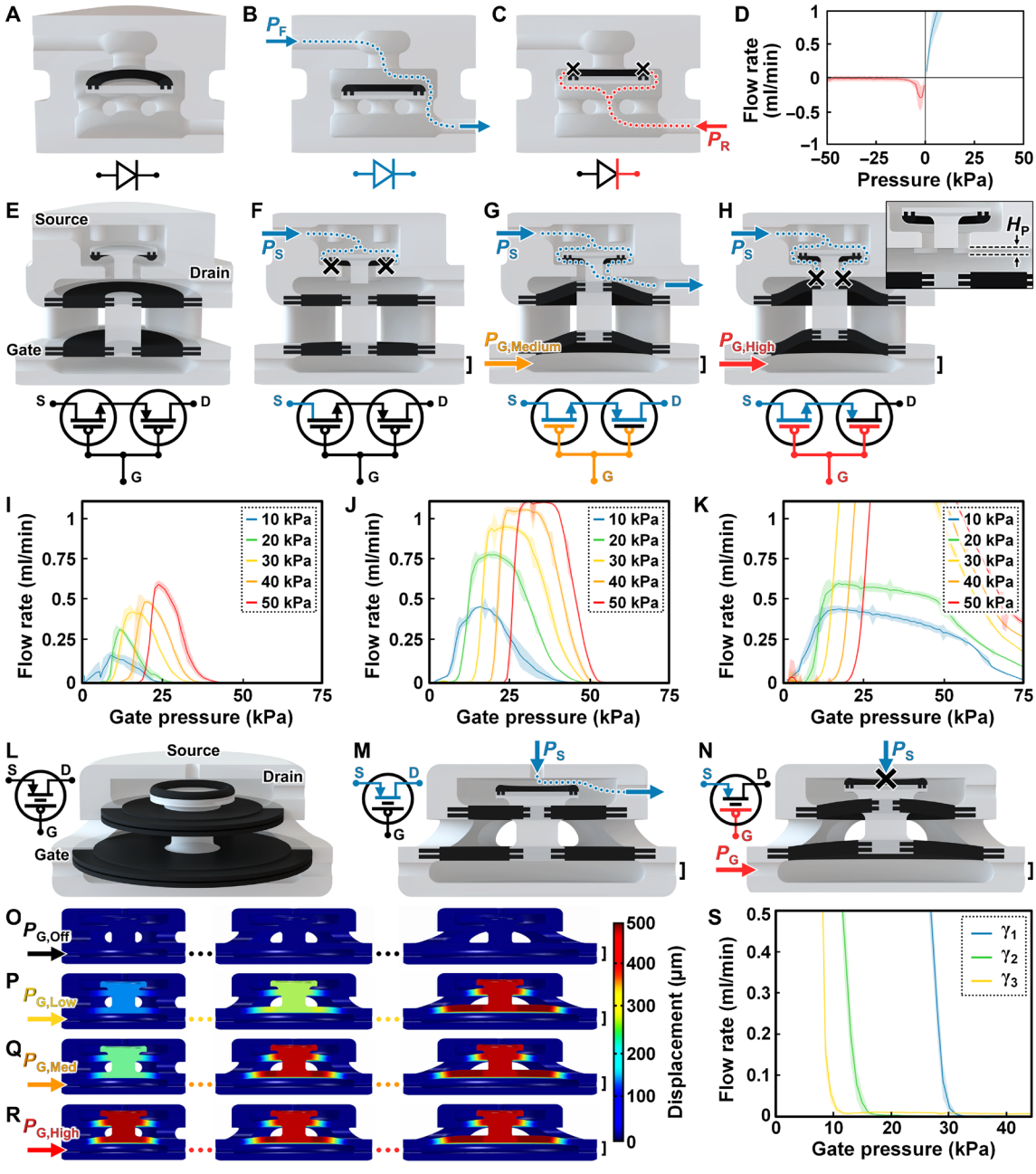

Fig. 2. Operating principles and results for PolyJet 3D printing–based fluidic circuit elements comprising integrated compliant (black) and rigid (white) materials. (**A** to **C**) Conceptual illustrations of the (A) architecture, (B) "forward flow" state, and (C) "reverse flow" state for the fluidic diode. (**D**) Experimental results for directional fluid flow versus pressure for the fluidic diode. (**E** to **H**) Conceptual illustrations of the (E) architecture, (F) "closed" state [induced by a source pressure (P_S) input], (G) "open" state [facilitated by a gate pressure (P_G) input of sufficient magnitude], and (H) "reclosed" state (caused by a high P_G input) for the normally closed fluidic transistor. The reclosed state dynamics can be adjusted by tuning the post height (H_P). (**I** to **K**) Experimental results for source-to-drain fluid flow (Q_{SD}) versus P_G corresponding to distinct, constant P_S inputs for normally closed fluidic transistors designed with H_P = (I) 0 μm, (J) 250 μm, and (K) 500 μm. (**L** to **N**) Conceptual illustrations of the (L) architecture, (M) open state, and (N) closed state (facilitated by a P_G input of sufficient magnitude) for a normally open fluidic transistor. (**O** to **R**) Simulations of diaphragm displacement for fluidic transistors with diaphragm area ratios of (left) 1 (γ_1), (middle) 2 (γ_2), and (right) 3.5 (γ_3) for P_G = (O) 0 kPa, (P) 13 kPa, (Q) 23 kPa, and (R) 54 kPa. See also movie S2. (**S**) Experimental results for relative Q_{SD} versus P_G for normally open fluidic transistors with varying γ (P_S = 20 kPa) (see also fig. S1). All error bands denote SD.

is based on two primary states associated with the flow polarity. For the forward flow case, the free-floating disc is displaced away from the top orifice, allowing fluid to flow past the disc through the bottom orifices and out of the fluidic diode (Fig. 2B). When the flow polarity is reversed, however, the compliant O-ring of the sealing disc is brought into physical contact with the top surface of the central region, thereby obstructing the flow of fluid through the orifice (Fig. 2C).

We experimentally characterized the functionality of the fluidic diode by elucidating the flow behavior with respect to the input pressure magnitude and polarity (i.e., directionality) (Fig. 2D). Experimental results for the forward flow case revealed that increasing the input pressure produced a corresponding increase in the flow rate through the fluidic diode. For the reverse flow case in which a positive pressure was applied in the reverse direction (rather than a vacuum pressure applied at the inlet), the flow rate initially increased with increasing reverse pressure; however, this behavior appeared to inflect at approximately 3 kPa, with further increases in reverse pressure resulting in the flow rate decreasing. One potential basis for these results stems from the requirement for the free-floating sealing disc to first migrate toward the orifice and then for the O-ring to deform to promote sealing—phenomena that also account for the improvement in sealing performance at higher reverse pressures. Nonetheless, the experimental results revealed that the fluidic diode exhibited significant forward bias of the flow polarity (Fig. 2D).

As both n- and p-channel transistors offer distinct benefits in various electronics scenarios, here, we present fluidic circuit elements designed to yield functionalities that are analogous to each. To achieve a normally closed fluidic transistor that mimics the operation of an n-channel MOSFET in series with a p-channel MOSFET (both biased in the triode region), we designed a fluidic circuit element architecture that consists of three main components: (i) a rigid material structural casing as well as separate internal channels that include an upper source-to-drain region (with a single central orifice) and a bottom gate region, (ii) a free-floating sealing disc with a central post (extended from the bottom surface through the orifice) that is primarily composed of a rigid material but includes a compliant material O-ring beneath the bottom surface of the disc, and (iii) two compliant material diaphragms—corresponding to the source-to-drain and gate regions—connected to one another via a central rigid material piston (Fig. 2E). In response to an applied source pressure (P_S), the compliant O-ring of the free-floating component seals atop the surface adjacent to the orifice, thereby blocking the flow of fluid from the source input to the drain output (Q_{SD}) (Fig. 2F). Under the application of a gate pressure (P_G) of sufficient magnitude, the diaphragms deform such that the top surface of the central piston (connected to the source-to-drain region diaphragm) physically elevates the free-floating component to break the fluidic seal and, in turn, facilitate Q_{SD} (Fig. 2G). By increasing the P_G input further, however, the central piston's top surface approaches the orifice to obstruct Q_{SD} (Fig. 2H). Notably, the propensity for this fluidic pathway to be reclosed can be tuned by increasing the height of posts (H_P) arrayed surrounding the bottom surface of the orifice to physically prevent the top surface of the piston from approaching the orifice (Fig. 2H).

To interrogate the underlying relationships connecting the P_G and P_S inputs, H_P, and the resulting Q_{SD}, we printed and characterized normally closed fluidic transistors designed with H_P dimensions of 0, 250, and 500 μm (Fig. 2, I to K). Experiments for the 0-μm case revealed three overall trends. First, increases in the P_S input corresponded to a higher P_G magnitude required to transition from the "closed" state to the "open" state (Fig. 2I). Second, increasing the P_G input initially coincided with Q_{SD} increasing, but after reaching a maximum peak, further increases in P_G yielded reductions in Q_{SD} until the transition to the "reclosed" state appeared to be complete (i.e., fully obstructing Q_{SD}). Last, the magnitude and range associated with the open state increased with higher P_S inputs (Fig. 2I). Although several of the general behaviors for the 250- and 500-μm cases were similar to those of the 0-μm results, the most notable difference was the change in the open state behavior (Fig. 2, I to K). Specifically, the range of P_G inputs associated with open state performance broadened substantially with increasing H_P such that, for the 500-μm case, none of the P_S and P_G inputs tested corresponded to a fully reclosed state as observed for the 0- and 250-μm cases (Fig. 2, I to K). In combination, these results suggest that H_P provides an effective geometric means to transition the functionality of the normally closed fluidic transistor from exhibiting behaviors analogous to an n- and p-channel transistor in series to those more akin to solely an n-channel transistor.

To achieve a normally open fluidic transistor with operating characteristics that resemble a p-channel MOSFET (biased in the triode region), we designed an architecture with two key differences from that of the normally closed element (Fig. 2L). Although the source-to-drain and gate region diaphragms remain connected via an intervening rigid piston, the piston extends above the source-to-drain region diaphragm to bring its top surface closer to the source orifice. In addition, the compliant material O-ring is placed atop the piston (which eliminates the need for an internal region above the orifice) (Fig. 2L). In the absence of a P_G input, Q_{SD} is unobstructed (Fig. 2M); however, by applying a P_G input of sufficient magnitude, Q_{SD} can be fully blocked (Fig. 2N). A key feature of this fluidic transistor architecture is the fluidic separation of the source-to-drain and gate regions, which leads to a force balance on the intervening piston based on the product of each region pressure and corresponding diaphragm area. Thus, by designing the gate region diaphragm area (A_G) to be larger than the source-to-drain region diaphragm area (A_{SD}), a lower P_G is able to overcome a higher P_S to actuate the piston and physically obstruct Q_{SD}—a distinguishing property referred to as pressure-gain (γ) (*23*). Notably, these γ characteristics can be tuned geometrically by adjusting the ratio of A_G to A_{SD}.

We used theoretical and experimental methods to investigate the performance of fluidic transistors with identical source-to-drain regions, but differing A_G dimensions that correspond to A_G/A_{SD} ratios of 1 (γ_1), 2 (γ_2), and 3.5 (γ_3). Finite element analysis (FEA) simulations of the fluidic transistors revealed four fundamental states based on the P_G input: (i) $P_{G,Off}$, with each sealing O-ring remaining a distance of 500 μm from the top source input surface (Fig. 2O); (ii) $P_{G,Low}$, with only the γ_3 fluidic transistor in the sealed state (Fig. 2P); (iii) $P_{G,Medium}$, with the addition of the γ_2 fluidic transistor sealing (Fig. 2Q); and (iv) $P_{G,High}$, with all three fluidic transistors in sealed states (Fig. 2R and movie S2). Experiments with printed fluidic transistors revealed results consistent with the simulations, with larger γ properties leading to sealed-state behavior at lower P_G versus smaller γ designs (Fig. 2S and fig. S1). For example, under a constant P_S input of 20 kPa, obstruction of Q_{SD} occurred at P_G inputs of 10.1 ± 0.3, 14.9 ± 0.6, and 29.8 ± 0.5 kPa for the γ_3, γ_2, and γ_1 fluidic transistors, respectively (Fig. 2S). For the γ_1 case, the

requirement for the P_G magnitude to be larger than that of the P_S input to enter the closed state is likely due to the additional deformation required for the diaphragm to physically displace approximately 500 μm to seal the source orifice. For the γ_2 and γ_3 fluidic transistors, however, smaller P_G inputs were able to overcome larger P_S inputs even accounting for the additional diaphragm deformation required for sealing (Fig. 2S).

Constant flow–based soft robotic turtle

The ability for soft robots to execute periodic operations autonomously in response to constant fluidic inputs serves as a critical benchmark for fluidic circuitry–based systems (*13*, *17*, *24*–*26*). To evaluate such capabilities for the strategy presented in this work, we designed a soft robotic turtle with an integrated fluidic oscillator circuit—consisting of fluidic diodes and normally closed fluidic transistors (H_P = 250 μm)—with outputs connected to distinct, asymmetric bellowed soft actuators or "limbs" (Figs. 1B and 3, A to F). Under identical constant-flow conditions for fluid loaded via two distinct inlets, the embedded oscillator circuit repeatedly transitions through six primary states (Fig. 3, A to F). When one of the fluidic transistors enters its closed configuration (i.e., with the O-ring obstructing Q_{SD}), inputted fluid builds up in the upstream gate region of the opposing fluidic transistor until that element reaches the open configuration, allowing fluid to flow through the fluidic transistor and the fluidic diode to inflate the respective limb (Fig. 3A). As fluid flows into the pathway with the closed fluidic transistor, the constantly inputted fluid continues to inflate the gate diaphragm of the opposing fluidic transistor, which begins to progress to its reclosed configuration (Fig. 3B). As this process continues, the hydraulic resistance through the "reclosing" fluidic transistor increases (while Q_{SD} decreases), which causes inputted fluid to instead build up in the gate region of the initially closed configuration fluidic transistor (Fig. 3B). Ultimately, the initially closed fluidic transistor enters the open configuration, which not only causes the corresponding limb to inflate (Fig. 3C) but also allows for the fluid in the upstream gate region to displace, thereby inducing the opposing fluidic transistor to shift rapidly from the reclosed configuration (Fig. 3C) back to the closed configuration (Fig. 3D). Thereafter, the process repeats itself in the opposite orientation (Fig. 3, D to F) and then continues cycling in a periodic manner (Fig. 3, A to F).

To experimentally investigate the oscillating performance of the soft robotic turtle, we printed the unified soft robot in a single run via PolyJet 3D printing (Fig. 1, D to F, and movie S1). We applied a constant fluidic input with a flow rate set at 10 ml/min into both input ports while ensuring that the exhaust ports located at the tops of the fingers were not fluidically sealed for consistency with previous reports in the literature (*17*). During experimentation, the soft limbs exhibited continuous, periodic actuations that were distinct from one another, despite the identical constant input conditions (Fig. 3G). We used digital image correlation (DIC) processing software to quantify the deformation behaviors, which revealed the oscillations to be 75° out of phase (Fig. 3H). One potential basis for such behaviors is the use of the normally closed fluidic transistor, which plays a critical role in the oscillator circuit. As such, it is expected that varying the geometric parameters of the fluidic circuit element—for example, by adjusting H_P or altering the gate diaphragm dimensions to yield γ functionalities—could provide a means to readily tune the oscillation behaviors of soft robots.

Sinusoidal input–based soft robotic turtle

A wide range of systems in both conventional robotics and soft robotics fields are designed with respect to AC electrical signals (*45*). In this work, we explore the use of a fluidic analog in the form of oscillating fluidic input conditions as the mechanism for driving the periodic motions of a soft robotic turtle's "flippers." Each flipper is attached to four symmetric bellowed soft actuators connected both at the base and at the tips (Fig. 4A). Previously, researchers have demonstrated the use of PolyJet-based bellowed soft legs anchored to one another to achieve rotational movements (*27*, *46*). Here, we advance this concept by connecting three of the four actuators to corresponding fluidic transistors to promote swimming-inspired motions based on a sinusoidal P_G input (Fig. 4, A to D). Specifically, the integrated fluidic circuit of the soft robotic turtle comprises three distinct normally open fluidic transistors that differ only in terms of their γ properties (Fig. 4A). Upstream of the source input corresponding to each fluidic transistor is a fluidic pathway to a respective set of designated soft actuators. In addition, each fluidic transistor is designed with two drain outputs, which are both connected to exhaust ports.

The operating principle of the soft robotic turtle is based on the application of a single oscillating P_G input, while the P_S input is set to a constant magnitude. When the oscillating P_G input is at its minimum magnitude, the P_S input primarily induces flow to the exhaust drains of the fluidic transistors rather than to the soft actuators, which are fluidically sealed at the tips (Fig. 4A). As the oscillating P_G input increases to a magnitude capable of exclusively activating the fluidic transistor with the largest γ properties (i.e., γ_3), the pathway to the element's exhaust ports (i.e., Q_{SD}) is obstructed, causing a portion of the P_S-induced flow to instead divert to the corresponding soft actuators (Fig. 4B). The resulting expansion of the activated fluidic transistor–associated soft actuators is designed to cause the flippers to move in a downward-backward trajectory (Fig. 4B). As the P_G magnitude continues increasing, both the γ_2 and γ_3 fluidic transistors activate and the resulting inflation of the two sets of corresponding soft actuators combines to induce a larger backward trajectory for the flippers (Fig. 4C). As the oscillating P_G input approaches its maximum peak, the final fluidic transistor activates, resulting in all flow diverting to the three sets of connected soft actuators, which is designed to cause the flippers to move to an upward-backward trajectory (Fig. 4D). Thereafter, the cycle repeats periodically with respect to the oscillating P_G input (Fig. 4, A to D).

Using the PolyJet 3D printing strategy, we printed the soft robotic turtle with the integrated sinusoidal input–based fluidic circuit in a single run as a unified entity (Fig. 4E). Initially, we characterized the deformation dynamics of the soft actuators under a constant P_S input of 40 kPa and varying P_G inputs up to 100 kPa (Fig. 4F). One caveat to the use of the compliant material for the entirety of the bellowed soft actuators is that the flexibility resulted in downward deformation before the onset of a P_G input. As a result, we did not visually observe the designed downward-backward trajectory at lower P_G inputs, with backward movement appearing to dominate instead until initiation of the upward-backward trajectory associated with higher P_G regimes (Fig. 4F). To investigate the performance with respect to an AC-inspired fluidic signal, we applied a constant P_S input of 60 kPa while simultaneously inputting a sinusoidal P_G that varied from 0 to 80 kPa with a frequency of 0.1 Hz. We used DIC processing methods to track and quantify the displacements during experimentation, which revealed a difference between the

inflation-associated displacement path and that of the deflation routines, despite identical P_G inputs (Fig. 4G). One possible basis for this behavior is that, similar to the time required to discharge an electronic capacitor, a time delay associated with the deflation of the soft actuators could contribute to the flippers following a deflation path that is distinct from the inflation cycle. As soft actuators similar to those in this work are widely used in the soft robotics community, such phenomena could prove useful in enhancing self-regulating functionalities for soft robots under sinusoidal or other forms of periodic driving inputs.

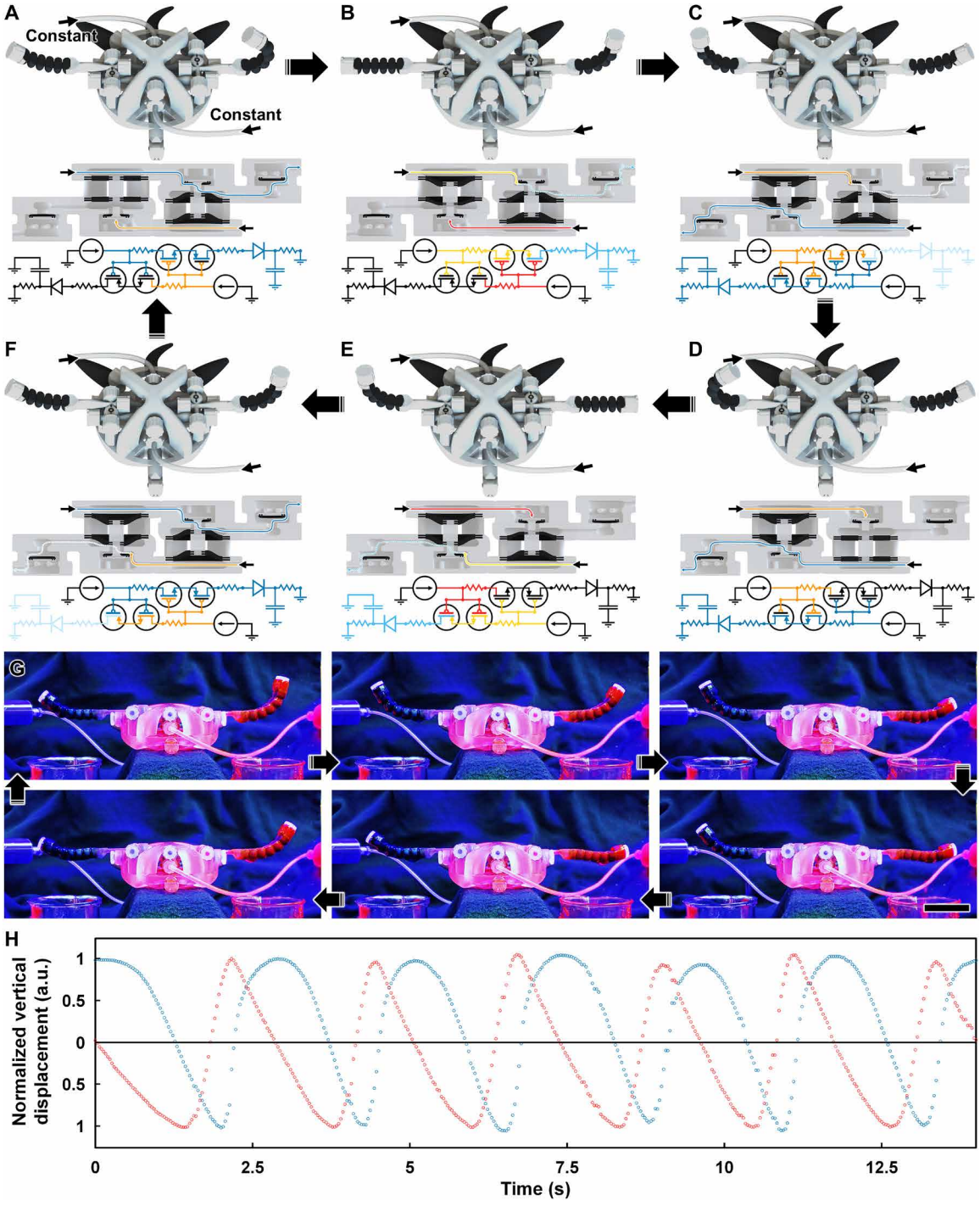

Fig. 3. Operating principle and experimental results for a constant flow–based soft robotic turtle. (**A** to **F**) Conceptual illustrations of the soft robot, the integrated fluidic oscillator circuit, and analogous circuit diagrams corresponding to the six primary states based on constant-flow input conditions. (**G**) Experimental results for soft robot functionality under constant-flow conditions (10 ml/min) during a representative operational period. Scale bar, 3 cm; see also movie S3. Photo credits: Ruben Acevedo, University of Maryland College Park. (**H**) Quantified experimental results for normalized vertical deformation of each soft actuating limb versus time under constant-flow conditions (10 ml/min). Blue, left limb; red, right limb. a.u., arbitrary unit.

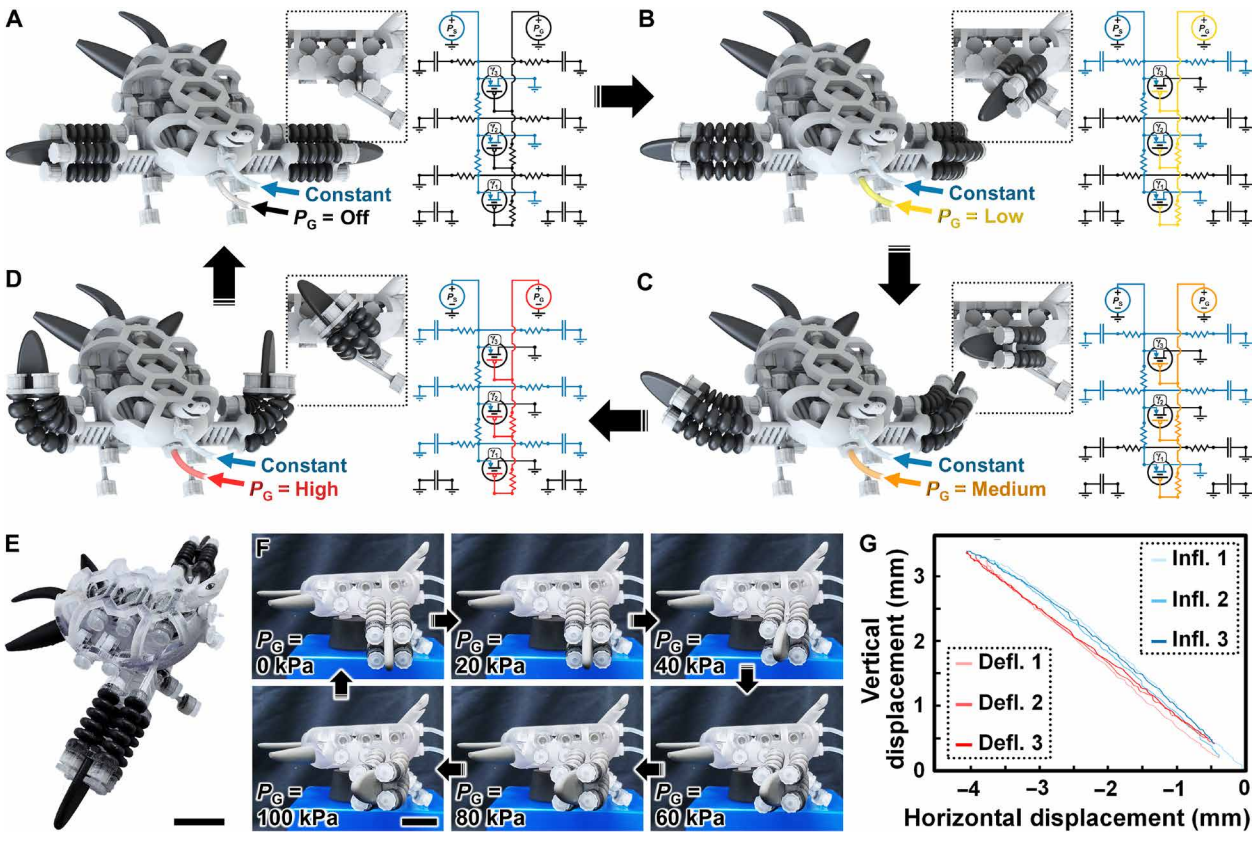

Fig. 4. Operating principle and experimental results for a sinusoidal input–based soft robotic turtle. (**A** to **D**) Conceptual illustrations and analogous circuit diagrams of the four primary states based on sinusoidal P_G input conditions and a constant P_S input. The integrated normally open fluidic transistors include distinct γ properties ($\gamma_1 < \gamma_2 < \gamma_3$). (**E**) Fabrication results. Scale bar, 2 cm. Photo credits: Ruben Acevedo, University of Maryland College Park. (**F**) Experimental results for soft actuator–associated flipper displacements corresponding to a constant P_S input of 40 kPa and varying P_G input. (**G**) DIC-processed experimental results of the flipper displacement path under a constant P_S input of 60 kPa and a sinusoidal P_G input that oscillated from 0 to 80 kPa with a frequency of 0.1 Hz. Blue and red denote inflation- and deflation-associated displacement cycles, respectively.

Programmed periodic input-based soft robotic hand

To explore the concept of a PolyJet-based soft robot capable of operating in response to a varying aperiodic fluidic input based on a set program, we investigated a soft robotic "hand" with integrated fluidic circuitry designed for an exemplar: playing the Nintendo Entertainment System (NES) Super Mario Bros. video game in real time using a controller (Fig. 5). The underlying fluidic circuit comprises normally open fluidic transistors with differing pressure-gain properties—with each source input connected to a corresponding soft actuating "finger"—that yields target operations based on the magnitude of a single, preprogrammed P_G input (while a P_S input remains constant). In the absence of a P_G input, P_S-based flow mainly bypasses the soft fingers and instead travels through the source-to-drain regions of each fluidic transistor and out of the system via each drain's exhaust port (Fig. 5A). For a characteristically low P_G input, however, the fluidic transistor with the largest γ properties closes, preventing flow out of the exhaust drain. As a result, a portion of the P_S is instead directed to the corresponding soft finger, which actuates to press the directional pad ("D-pad") of the controller (Fig. 5B). For a slightly higher P_G input, the fluidic transistor with the next largest γ closes, resulting in activation of both the D-pad and the "B" button of the NES controller (but not the "A" button) (Fig. 5C). Last, under a high P_G input, the fluidic transistor with the smallest γ properties finally closes, causing all three soft fingers to press their corresponding controller targets (Fig. 5D).

For the soft robotic hand, we designed bioinspired multimaterial soft robotic fingers that leverage the differences in rigidity of the two printed materials to emulate the bending behaviors of a human finger, including (i) the nonbending portions of the finger (phalanges) and their internal fluidic channels printed using a rigid material, and (ii) the inflatable "knuckle" components printed using a compliant material. Because of the asymmetric design of the bellowed soft knuckle components, as they inflate, the larger top portion expansion results in a downward actuation of the fingertip to exert a complementary force (Fig. 5, E and F; fig. S2; and movie S4).

We performed pneumatic experiments with independent soft finger–fluidic transistor systems to quantify the magnitude of the fingertip actuation force with respect to the P_S and P_G inputs as well as the γ properties of the integrated fluidic transistor (Supplementary Text and fig. S3). The experimental results revealed that the extent of the actuation force was directly related to the magnitude of the P_S input but, more importantly, that the soft fingers integrated with fluidic transistors with larger γ designs exhibited higher actuation forces at lower P_G inputs compared to their smaller γ counterparts (Fig. 5G and fig. S3). For example, exerting a force of 125 mN under a P_S input of 10 kPa required a P_G input of 19.2 ± 3.2,

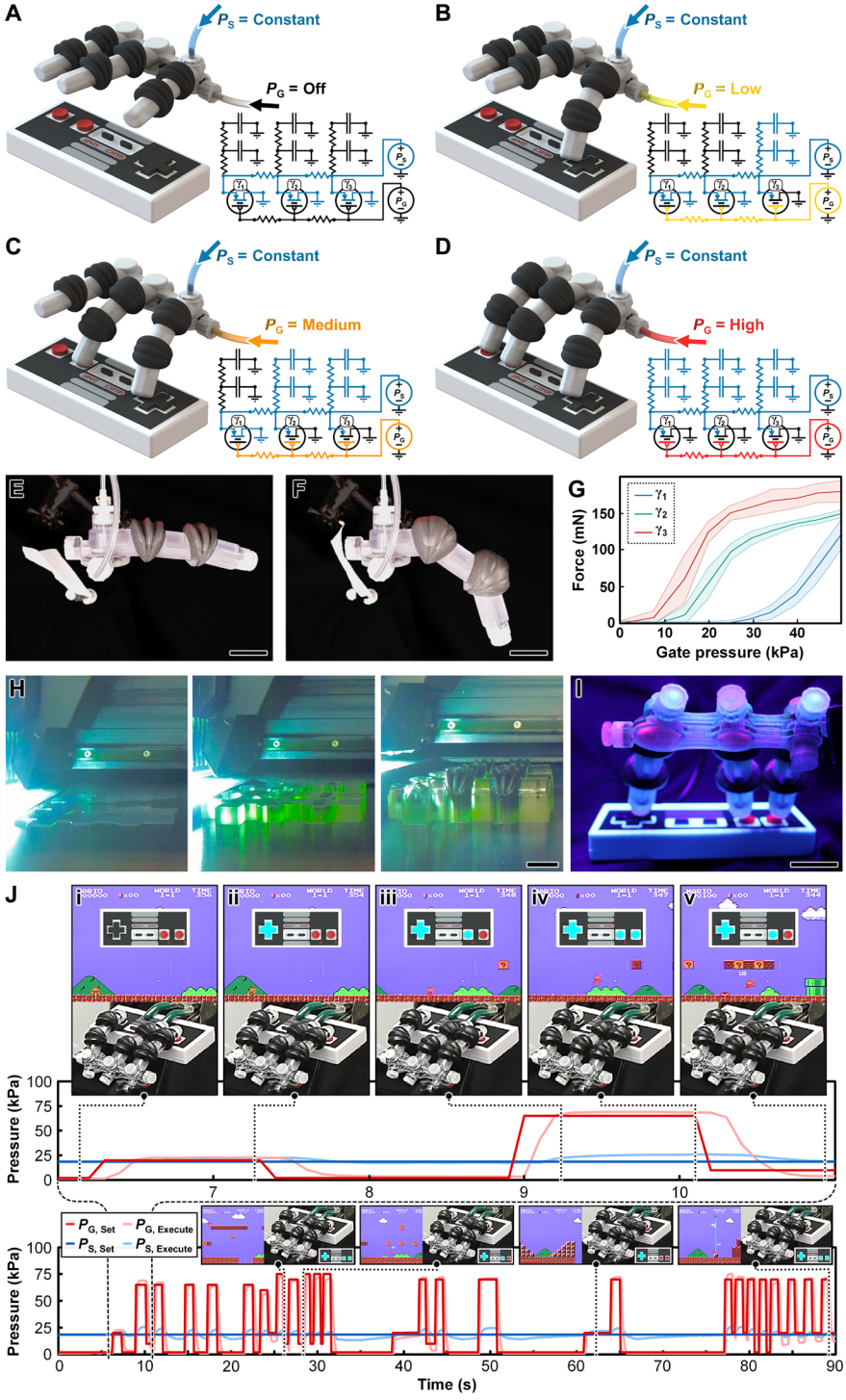

Fig. 5. Concepts and results for a preprogrammed, aperiodic fluidic input–based soft robotic hand with integrated fluidic circuitry. (**A** to **D**) Conceptual illustrations and analogous circuit diagrams of the four primary states based on distinct P_G magnitudes, while a P_S input remains constant. The integrated normally open fluidic transistors include distinct γ properties ($\gamma_1 < \gamma_2 < \gamma_3$). (**E** and **F**) Experimental results for a soft robotic finger with an integrated γ_3 fluidic transistor for P_S = 20 kPa and P_G = (E) 0 kPa and (F) 20 kPa. Scale bars, 2 cm; see also movie S4. Photo credits: Kristen M. Edwards, Jennifer Landry, and Ryan D. Sochol, University of Maryland College Park. (**G**) Quantified experimental results for fingertip actuation force versus P_G for soft robotic finger–fluidic transistor systems with varying γ and P_S of 10 kPa. Error bands denote SD. (**H**) Sequential time-lapse images of the PolyJet 3D printing process. Scale bar, 2 cm; see also movie S5. Photo credit: Joshua D. Hubbard, University of Maryland, College Park. (**I**) Fabrication results. Scale bar, 2 cm. Photo credit: Joshua D. Hubbard and Kristen M. Edwards, University of Maryland, College Park. (**J**) Experimental results for completing the first level of the Super Mario Bros. video game in real time in response to a preprogrammed P_G input (P_S programmed to remain constant). Callouts include the controller activation state, the game state, and an image of the soft robotic hand using the controller corresponding to demonstrative time points; see also movie S6. Photo credit: Joshua D. Hubbard, Ruben Acevedo and Kristen M. Edwards, University of Maryland, College Park.

32.6 ± 6.5, and 48.5 ± 4.0 kPa for the γ_3, γ_2, and γ_1 fluidic transistors, respectively (Fig. 5G).

Following the manufacturing process (Fig. 5H and movie S5), we affixed the fingertips of the PolyJet-printed soft robotic hand to their respective target locations of the NES controller to limit lateral deflections caused by the shapes of the buttons (Fig. 5I). For the controller used in this work, a constant P_S input of 18.5 kPa allowed for four operational states: (i) $P_{G,Off} \leq 5$ kPa, none of the buttons are pressed—Mario is immobile (Fig. 5Ji); (ii) $P_{G,Low} \geq 20$ kPa, the right button of the D-pad is pressed—Mario walks (Fig. 5Ji); (iii) $P_{G,Medium} \geq 40$ kPa, the B button is also pressed—Mario runs (Fig. 5Jiii); and (iv) $P_{G,High} \geq 60$ kPa, all of the buttons are pressed—Mario jumps (Fig. 5Jiv). One caveat to the use of soft actuating fingers is that, similar to the time required to charge or discharge an electronic capacitor, the soft knuckle components exhibited analogous time delays when executing the inflation (e.g., Fig. 5J, ii and iv) and deflation (e.g., Fig. 5Jv) routines that underlie actuation force. By taking such factors into consideration in designing the program that dictates the varying aperiodic P_G input, the soft robotic hand was able to complete the first level of Super Mario Bros. in real time (Fig. 5J and movie S6).

DISCUSSION

Fluidic circuitry provides powerful means to enhance soft robot autonomy and, in turn, reduce and/or eliminate the tethering requirements associated with conventional fluidic control schemes (*47*). In this work, we introduced the concept of additively manufacturing unified soft robotic systems with fully integrated fluidic circuitry in a single print run. To support the sophistication of the underlying fluidic circuits that govern the soft robot functionalities, we also presented and characterized a fundamental class of fluidic circuit elements that are compatible with the PolyJet 3D printing strategy, including fluidic diodes as well as normally closed and normally open fluidic transistors. Historically, it has been difficult to achieve and/or customize γ properties for conventionally manufactured fluidic operators (*24*). Thus, a particularly important feature of both sets of fluidic transistors reported here stems from the distinct source-to-drain and gate region diaphragms connected via an intervening piston, which allows for γ-associated behaviors to be tuned through straightforward geometric means (i.e., the ratio of the diaphragm diameters) as desired. Experimental results revealed that the fluidic circuit elements exhibited performance characteristics consistent with their electrical counterparts both independently and when integrated as part of larger integrated fluidic circuits. Although the fluidic circuits in this work were designed with respect to soft robots, it should be noted that fluidic valving and routing capabilities are widely used in chemical, biological, and biomedical fields (*48*), and thus, the fluidic processing approaches demonstrated here could be extended to support such applications.

As the area of soft robotics is still relatively nascent, potential input modalities for driving soft robot operations remain diverse. Thus, in this work, we focused on investigating soft robots with integrated fluidic circuits based on inputs inspired by electrical signals associated with conventional robotics fields. First, we printed a soft robotic turtle capable of converting constant-flow inputs—analogous to DC electrical signals—to periodic, out-of-phase oscillations of its distinct limbs. We also designed and printed a distinct soft robotic turtle that generated periodic motions of its flippers under sinusoidal fluidic input conditions—analogous to AC electrical signals—based on an integrated fluidic circuit consisting of fluidic transistors with varying γ properties.

In addition, we took advantage of such γ-enabled functionalities to create a soft robotic hand capable of hard-coded operations based primarily on the magnitude of a single, preprogrammed control input—akin to variable current electrical signals. We used a set pressure input program to autonomously control the soft robotic hand, resulting in target actuators pressing and depressing the buttons of an NES controller at specific times to complete the first level of the original Super Mario Bros. video game in real time. Although this use case served as an exemplar, the γ-based approach for controlling the fingers of the soft robotic hand could be extended to minimize the tethering requirements for emerging applications such as soft robotic gloves and rehabilitation devices (*5*, *49*, *50*). Furthermore, in contrast to conventional standards for evaluating soft robot capabilities that lack stringent performance metrics or associated penalties, the Super Mario Bros. demonstration is constrained with respect to externally established and invariable conditions (i.e., timing and level makeup) for which a single missed or inaccurately executed operation can result in complete failure. Given the recent concerns in the field of soft robotics regarding quantitative utility (*51*), we propose that future works should consider similar means of assessment that are founded on externally dictated, unyielding operational demands.

Among the soft robots presented in this work, the constant flow–based soft robotic turtle is best suited to serve as a point of reference for comparing distinct methodologies for manufacturing fluidic circuit-based soft robots, as its oscillating behaviors are consistent with those often reported in the literature by other groups (*15*, *17*, *24*–*27*). For example, in contrast to soft lithography–based protocols previously used for fluidic circuit fabrication (*13*, *15*–*17*), which typically necessitate technical training and access to microfabrication equipment and clean room facilities (*19*, *52*), access to a PolyJet 3D printer (either directly or through a commercial 3D printing service) represents the only critical barrier to reproducing all of the soft robots and integrated fluidic circuits reported here. Although the support material removal protocols of the presented PolyJet-based strategy require a degree of manual labor (on the order of tens of minutes, e.g., movie S7), the elimination of essentially all other manual fabrication, integration, and assembly procedures associated with soft robotic actuators, structural/body features, and fluidic circuitry is a central benefit. In addition, as such manual protocols can lead to differences in performance based on user skill and training, it is expected that the automated PolyJet 3D printing process could provide advantages in terms of robot-to-robot repeatability while reducing failures caused by user error during manufacturing. It is important to note that the reported strategy could be improved further by applying recent techniques that instead use noncuring liquid-based support materials (*40*, *44*)—with the caveat that such actions typically void the warranty of the 3D printer—to circumvent the vast majority of the support removal protocols used here. Such adaptations could, however, negatively affect the integrity of the multimaterial interfaces and/or operator-to-operator and, in turn, robot-to-robot efficacy and reproducibility. Thus, such endeavors should be undertaken with a high degree of caution.

Although all of the fluidic circuit elements and soft robots were designed and fabricated as multimaterial entities, for applications that require entirely soft robots, the rigid materials could be replaced

with compliant materials as desired. Similarly, the presented approach is not exclusively limited to PolyJet 3D printing and could be adapted for alternative additive technologies, such as using direct laser writing–based fluidic circuit elements (*53*–*55*) for soft microrobots or stereolithography-compatible soft materials (*56*) for meso-/macroscale systems. Nonetheless, the PolyJet-based strategy presented here offers distinctive promise to enhance accessibility within the field of soft robotics while supporting a level of reproducibility and design versatility (e.g., for the fluidic operators, integrated fluidic circuits, and the overall architectures of unified soft robotic systems) that has not been reported for alternative methodologies. Specifically, as the models for all of the fundamental fluidic circuit elements and soft robots in this work are available online (see the Supplementary Materials), researchers can readily download, modify on demand, and/or reproduce (e.g., 3D-print on site or via a commercial 3D printing service) all of the capabilities demonstrated here, thereby providing a new pathway for researchers spanning broad academic backgrounds to design, additively manufacture, and advance soft robotic systems that comprise fully integrated fluidic circuitry.

MATERIALS AND METHODS

PolyJet 3D printing–based fabrication

The designs and protocols for additively manufacturing all of the components and systems in this work were based on the use of an Objet500 Connex3 PolyJet 3D printer (Stratasys, Eden Prairie, MN) and are similar to those reported in our previous work (*57*). Initially, all of the fluidic circuit elements, soft actuators, ports, and integrated soft robotic systems were modeled using the CAD software SolidWorks (Dassault Systèmes SE, France). The ports were designed to be compatible with polycarbonate barbed luer adapters (EW-45501-00, Cole-Parmer, Vernon Hills, IL). Each model was exported as two self-referenced STL files corresponding to either the rigid or compliant print materials; the sacrificial support material is autogenerated in the computer-aided manufacturing (CAM) software and, thus, does not require an associated STL file. Before the PolyJet 3D printing process, the STL files corresponding to the distinct materials were imported into the Stratasys CAM software, GrabCAD Print, for slicing corresponding to layer heights of 30 μm and respective material assignments.

The materials used for PolyJet 3D printing included (i) MED610 (Stratasys) for the rigid photoplastic material, (ii) Agilus30 (Stratasys) for the compliant photopolymer material, and (iii) SUP706 (Stratasys) for the water-soluble sacrificial support material. For the systems presented in this work, the PolyJet build time ranged from approximately 3 hours (e.g., movie S5) to 8 hours (e.g., movie S1), with structure height (i.e., total number of distinct layers) representing the key determinant in the print time. Following the completion of the PolyJet-based additive manufacturing process, printed components and systems—weakly adhered to the build plate through a raft of sacrificial support material—were detached manually (i.e., by hand using a scraper).

Because the PolyJet printing process includes the deposition of a sacrificial support material not only underneath external regions but also within internal voids of printed devices (e.g., in the enclosed fluidic networks), we developed and used protocols to facilitate removal of the sacrificial support material from all locations. Initially, easily accessible external support material was removed manually (i.e., by hand). A metal rod (1 mm in diameter) was inserted through each channel (e.g., via a Dremel 4300) to displace a portion of the embedded support material while opening a pathway for syringe-based infusion with deionized (DI) water. Thereafter, the prints were submerged in a bath of 2% NaOH and 2% Na_2SiO_3 (w/w) in DI water (with continuous magnetic stirring), while the NaOH-Na_2SiO_3 solution was continuously pumped through the channels using peristaltic pumps (Gikfun, GuangDong, China) for up to 12 hours. Last, the prints were rinsed with DI water to remove residual solution from both internal and external regions. An example of the support removal process for the integrated fluidic oscillator circuit is presented in movie S7. It is important to note that all of the devices in this work were designed in consideration of the support removal process, such as by including straight channel pathways with open ports on each side (to facilitate insertion of the metal rod). For cases in which such ports were superfluous to component functionality, polypropylene luer caps (EW-30800-12, Cole-Parmer) were used to seal the ports before use. In addition, for smaller modular components, the majority of the aforementioned manual protocols can be bypassed if desired (Supplementary Text and figs. S4 to S7).

FEA simulations

Theoretical simulations of the fluidic transistors were performed using the commercial FEA software COMSOL Multiphysics v.5.3a (COMSOL Inc., Sweden) via methods similar to those reported in our previous work (*57*). Initially, the complete 3D CAD model (i.e., including both materials fully assembled) corresponding to each fluidic transistor was imported into the FEA software, and then the distinct material properties were set for the compliant and rigid components. Specifically, the compliant components were modeled as Agilus30 (E = 0.09 GPa; $\rho = 1.125 \times 10^3$ kg/m^3; $\nu = 0.4$), while the rigid components were modeled as MED610 (E = 2.6 GPa; $\rho = 1.175 \times 10^3$ kg/m^3; $\nu = 0.7$). Simulations were performed using the COSMOL Multiphysics "Solid Mechanics" module. The P_G input was modeled as a boundary load on the internal surface of the gate region diaphragm, while the source-to-drain region diaphragm components were assigned as free boundaries. For all of the fluidic transistor designs modeled, the P_G input was incrementally increased up to the point of physical contact between the top surface of the sealing O-ring and the surface adjacent to the source orifice. All simulations were computed using the stationary (time-independent) solver and a parametric sweep function for applied loads.

Fluidic circuit element experimentation

All fluidic circuit element experiments were performed using the Fluigent Microfluidic Control System (MFCS) and Flow-Rate Platform (FRP) along with the corresponding Scite and MAESFLO software (Fluigent, Paris, France). Input pressures were applied through fluorinated ethylene propylene (Cole-Parmer, Vernon Hills, IL) and silicone rubber (1/8″, McMaster-Carr, Elmhurst, IL) tubing connected to polycarbonate barbed luer adapters (EW-45501-00, Cole-Parmer), which were directly interfaced with the complementary designed ports of the components. For fluidic experimentation, pressurized air was inputted into the gate regions of the fluidic transistors, while DI water was used as the input fluid for source regions of the fluidic transistors and for both directions of the fluidic diodes. Flow rates were measured using Fluigent flow unit flow sensors (models L and XL). All experiments were conducted under room temperature environment (20° to 25°C). The results were processed, quantified, and plotted using MATLAB 9.6 (MathWorks, Natick, MA),

with data binning techniques used to discretize the raw continuous datasets into small interval bins for analysis. Experimental results are presented in the text as means ± SD.

Soft robot experimentation

Experiments with the constant flow–based soft robotic turtle were performed using two syringe pumps (NE-300, New Era Pump Systems Inc., Farmingdale, NY) set at 10.0 ml/min to drive fluid into two distinct inlet ports. All other ports were sealed using luer caps (EW-30800-12, Cole-Parmer), with the exception of the outlet ports at the end of each finger, which were not fluidically sealed to serve as fluidic outlets. Experiments with the sinusoidal input–based soft robotic turtle were performed using a Fluigent Flow-EZ Module with a preprogrammed sinusoidal pressure output (peak-to-peak amplitude = 80 kPa; frequency = 0.1 Hz) for the P_G input and a separate module set at a constant magnitude of 60 kPa for the P_S input. All other ports were sealed using luer caps (EW-30800-12, Cole-Parmer), with the exception of the exhaust ports connected to the drain outlets of the fluidic transistors. To quantify the displacement dynamics from videos recorded for both soft robotic turtles during experimental testing, the DIC software VIC-2D (Correlated Solutions, Irmo, SC) was used for tracking and analysis. Subset and step sizes of 35 and 9, respectively, were used for the analysis along with a zero-normalized squared differences criterion, with incremental correlation and exhaustive search enabled.

Before experimentation with the integrated soft robotic hand, pneumatic experiments with varying P_S and P_G inputs were performed using three distinct soft robotic finger–fluidic transistor systems, differing only in terms of the fluidic transistor γ properties (i.e., γ_1, γ_2, and γ_3), to quantify the actuation force at the fingertip (Supplementary Text). Force measurements were obtained using a miniature S-Beam load cell (LFS 270-M3 5, Cooper Instruments & Systems, Warrenton, VA), with the signal amplified using a DCM 465 Current Bridge Amplifier (Cooper Instruments & Systems) and digitized with a USB-6009 data acquisition (DAQ) device (National Instruments, Austin, TX). All force data were recorded using SignalExpress software (National Instruments).

For experiments with the soft robotic hand, the overall component was fixed in place using a clamp, while the base of each fingertip was affixed to the corresponding NES controller button using hot glue (AdTech Mini, Merchant General Corp., Oldsmar, FL) such that (i) the γ_3 fluidic transistor–associated soft robotic finger was coupled to the right arrow button of the D-Pad, (ii) the γ_2 fluidic transistor–associated soft robotic finger was coupled to the B button, and (iii) the γ_1 fluidic transistor–associated soft robotic finger was coupled to the A button. In addition, the buttons of the NES controller (Nintendo, Japan, Kyoto) were modified by removing superfluous internal rubber elements to reduce the force necessary for activation without changing the base functionality. Pneumatic experiments with the soft robotic hand were performed by running a custom script—programmed with Fluigent Scite software—via the Fluigent MAESFLO software and MFCS to dynamically regulate the P_G input while maintaining a constant P_S. With the exception of the source and gate input ports as well as the drain-associated exhaust ports, all other ports were sealed using luer caps (EW-30800-12, Cole-Parmer). All experiments were conducted under room temperature environment (20° to 25°C) and recorded using an EOS Rebel 1 camera (Canon, Tokyo, Japan).

SUPPLEMENTARY MATERIALS

Supplementary material for this article is available at http://advances.sciencemag.org/cgi/content/full/7/29/eabe5257/DC1

REFERENCES AND NOTES

1. R. F. Shepherd, F. Ilievski, W. Choi, S. A. Morin, A. A. Stokes, A. D. Mazzeo, X. Chen, M. Wang, G. M. Whitesides, Multigait soft robot. *Proc. Natl. Acad. Sci. U.S.A.* **108**, 20400–20403 (2011).
2. S. A. Morin, R. F. Shepherd, S. W. Kwok, A. A. Stokes, A. Nemiroski, G. M. Whitesides, Camouflage and display for soft machines. *Science* **337**, 828–832 (2012).
3. D. Rus, M. T. Tolley, Design, fabrication, and control of soft robots. *Nature* **521**, 467–475 (2015).
4. F. Ilievski, A. D. Mazzeo, R. F. Shepherd, X. Chen, G. M. Whitesides, Soft robotics for chemists. *Angew. Chem. Int. Ed.* **50**, 1890–1895 (2011).
5. P. Polygerinos, Z. Wang, K. C. Galloway, R. J. Wood, C. J. Walsh, Soft robotic glove for combined assistance and at-home rehabilitation. *Robot. Auton. Syst.* **73**, 135–143 (2015).
6. C. Laschi, B. Mazzolai, M. Cianchetti, Soft robotics: Technologies and systems pushing the boundaries of robot abilities. *Sci. Robot.* **1**, eaah3690 (2016).
7. B. Mosadegh, T. Bersano-Begey, J. Y. Park, M. A. Burns, S. Takayama, Next-generation integrated microfluidic circuits. *Lab Chip* **11**, 2813–2818 (2011).
8. P. Polygerinos, N. Correll, S. A. Morin, B. Mosadegh, C. D. Onal, K. Petersen, M. Cianchetti, M. T. Tolley, R. F. Shepherd, Soft robotics: Review of fluid-driven intrinsically soft devices; manufacturing, sensing, control, and applications in human-robot interaction. *Adv. Eng. Mater.* **19**, 1700016 (2017).
9. S. T. Mahon, J. O. Roberts, M. E. Sayed, D. H.-T. Chun, S. Aracri, R. M. Mc Kenzie, M. P. Nemitz, A. A. Stokes, Capability by stacking: The current design heuristic for soft robots. *Biomimetics* **3**, 16 (2018).
10. N. Vasios, A. J. Gross, S. Soifer, J. T. B. Overvelde, K. Bertoldi, Harnessing viscous flow to simplify the actuation of fluidic soft robots. *Soft Robot.* **7**, 1–9 (2020).
11. M. Garrad, G. Soter, A. T. Conn, H. Hauser, J. Rossiter, A soft matter computer for soft robots. *Sci. Robot.* **4**, eaaw6060 (2019).
12. M. P. Nemitz, C. K. Abrahamsson, L. Wille, A. A. Stokes, D. J. Preston, G. M. Whitesides, Soft non-volatile memory for non-electronic information storage in soft robots, in *2020 3rd IEEE International Conference on Soft Robotics (RoboSoft)* (IEEE, 2020), pp. 7–12.
13. Z. Li, S.-J. Kim, Autonomous microfluidic actuators for periodic sequential flow generation. *Sci. Adv.* **5**, eaat3080 (2019).
14. N. Napp, B. Araki, M. T. Tolley, R. Nagpal, R. J. Wood, Simple passive valves for addressable pneumatic actuation, in *2014 IEEE International Conference on Robotics and Automation (ICRA)* (IEEE, 2014), pp. 1440–1445.
15. T. Ranzani, S. Russo, N. W. Bartlett, M. Wehner, R. J. Wood, Increasing the dimensionality of soft microstructures through injection-induced self-folding. *Adv. Mater.* **30**, 1802739 (2018).
16. B. Mosadegh, C.-H. Kuo, Y.-C. Tung, Y.-S. Torisawa, T. Bersano-Begey, H. Tavana, S. Takayama, Integrated elastomeric components for autonomous regulation of sequential and oscillatory flow switching in microfluidic devices. *Nat. Phys.* **6**, 433–437 (2010).
17. M. Wehner, R. L. Truby, D. J. Fitzgerald, B. Mosadegh, G. M. Whitesides, J. A. Lewis, R. J. Wood, An integrated design and fabrication strategy for entirely soft, autonomous robots. *Nature* **536**, 451–455 (2016).
18. S. Chen, Y. Cao, M. Sarparast, H. Yuan, L. Dong, X. Tan, C. Cao, Soft crawling robots: Design, actuation, and locomotion. *Adv. Mater. Technol.* **5**, 1900837 (2020).
19. N. Bhattacharjee, A. Urrios, S. Kang, A. Folch, The upcoming 3D-printing revolution in microfluidics. *Lab Chip* **16**, 1720–1742 (2016).
20. M. A. Unger, H.-P. Chou, T. Thorsen, A. Scherer, S. R. Quake, Monolithic microfabricated valves and pumps by multilayer soft lithography. *Science* **288**, 113–116 (2000).
21. D. C. Leslie, C. J. Easley, E. Seker, J. M. Karlinsey, M. Utz, M. R. Begley, J. P. Landers, Frequency-specific flow control in microfluidic circuits with passive elastomeric features. *Nat. Phys.* **5**, 231–235 (2009).
22. P. N. Duncan, T. V. Nguyen, E. E. Hui, Pneumatic oscillator circuits for timing and control of integrated microfluidics. *Proc. Natl. Acad. Sci. U.S.A.* **110**, 18104–18109 (2013).
23. J. A. Weaver, J. Melin, D. Stark, S. R. Quake, M. A. Horowitz, Static control logic for microfluidic devices using pressure-gain valves. *Nat. Phys.* **6**, 218–223 (2010).
24. P. Rothemund, A. Ainla, L. Belding, D. J. Preston, S. Kurihara, Z. Suo, G. M. Whitesides, A soft, bistable valve for autonomous control of soft actuators. *Sci. Robot.* **3**, eaar7986 (2018).
25. D. J. Preston, H. J. Jiang, V. Sanchez, P. Rothemund, J. Rawson, M. P. Nemitz, W.-K. Lee, Z. Suo, C. J. Walsh, G. M. Whitesides, A soft ring oscillator. *Sci. Robot.* **4**, eaaw5496 (2019).
26. D. J. Preston, P. Rothemund, H. J. Jiang, M. P. Nemitz, J. Rawson, Z. Suo, G. M. Whitesides, Digital logic for soft devices. *Proc. Natl. Acad. Sci. U.S.A.* **116**, 7750–7759 (2019).
27. D. Drotman, S. Jadhav, D. Sharp, C. Chan, M. T. Tolley, Electronics-free pneumatic circuits for controlling soft-legged robots. *Sci. Robot.* **6**, eaay2627 (2021).

28. R. Z. Gao, C. L. Ren, Synergizing microfluidics with soft robotics: A perspective on miniaturization and future directions. *Biomicrofluidics* **15**, 011302 (2021).
29. M. Soreni-Harari, R. St Pierre, C. McCue, K. Moreno, S. Bergbreiter, Multimaterial 3D printing for microrobotic mechanisms. *Soft Robot.* **7**, 59–67 (2020).
30. Y.-F. Zhang, C. J.-X. Ng, Z. Chen, W. Zhang, S. Panjwani, K. Kowsari, H. Y. Yang, Q. Ge, Miniature pneumatic actuators for soft robots by high-resolution multimaterial 3D printing. *Adv. Mater. Technol.* **4**, 1900427 (2019).
31. M. A. Skylar-Scott, J. Mueller, C. W. Visser, J. A. Lewis, Voxelated soft matter via multimaterial multinozzle 3D printing. *Nature* **575**, 330–335 (2019).
32. A. K. Au, N. Bhattacharjee, L. F. Horowitz, T. C. Chang, A. Folch, 3D-printed microfluidic automation. *Lab Chip* **15**, 1934–1941 (2015).
33. C. I. Rogers, K. Qaderi, A. T. Woolley, G. P. Nordin, 3D printed microfluidic devices with integrated valves. *Biomicrofluidics* **9**, 016501 (2015).
34. R. D. Sochol, E. Sweet, C. C. Glick, S. Venkatesh, A. Avetisyan, K. F. Ekman, A. Raulinaitis, A. Tsai, A. Wienkers, K. Korner, K. Hanson, A. Long, B. J. Hightower, G. Slatton, D. C. Burnett, T. L. Massey, K. Iwai, L. P. Lee, K. S. J. Pister, L. Lin, 3D printed microfluidic circuitry via multijet-based additive manufacturing. *Lab Chip* **16**, 668–678 (2016).
35. A. V. Nielsen, M. J. Beauchamp, G. P. Nordin, A. T. Woolley, 3D printed microfluidics. *Annu. Rev. Anal. Chem.* **13**, 45–65 (2020).
36. R. Su, J. Wen, Q. Su, M. S. Wiederoder, S. J. Koester, J. R. Uzarski, M. C. McAlpine, 3D printed self-supporting elastomeric structures for multifunctional microfluidics. *Sci. Adv.* **6**, eabc9846 (2020).
37. A. Bruyas, F. Geiskopf, L. Meylheuc, P. Renaud, Combining multi-material rapid prototyping and pseudo-rigid body modeling for a new compliant mechanism, in *2014 IEEE International Conference on Robotics and Automation (ICRA)* (IEEE, 2014), pp. 3390–3396.
38. J. A. E. Hughes, P. Maiolino, F. Iida, An anthropomorphic soft skeleton hand exploiting conditional models for piano playing. *Sci. Robot.* **3**, eaau3098 (2018).
39. N. W. Bartlett, M. T. Tolley, J. T. B. Overvelde, J. C. Weaver, B. Mosadegh, K. Bertoldi, G. M. Whitesides, R. J. Wood, A 3D-printed, functionally graded soft robot powered by combustion. *Science* **349**, 161–165 (2015).
40. R. MacCurdy, R. Katzschmann, K. Youbin, D. Rus, Printable hydraulics: A method for fabricating robots by 3D co-printing solids and liquids, in *2016 IEEE International Conference on Robotics and Automation (ICRA)* (IEEE, 2016), pp. 3878–3885.
41. S. J. Keating, M. I. Gariboldi, W. G. Patrick, S. Sharma, D. S. Kong, N. Oxman, 3D-printed multimaterial microfluidic valve. *PLOS ONE* **11**, e0160624 (2016).
42. D. Drotman, M. Ishida, S. Jadhav, M. T. Tolley, Application-driven design of soft, 3D printed, pneumatic actuators with bellows. *IEEE/ASME Trans. Mechatron.* **24**, 78–87 (2019).
43. E. H. Childs, A. V. Latchman, A. C. Lamont, J. D. Hubbard, R. D. Sochol, Additive assembly for polyjet-based multimaterial 3D printed microfluidics. *J. Microelectromech. Syst.* **29**, 1094–1096 (2020).
44. A. D. Castiaux, C. W. Pinger, E. A. Hayter, M. E. Bunn, R. S. Martin, D. M. Spence, PolyJet 3D-printed enclosed microfluidic channels without photocurable supports. *Anal. Chem.* **91**, 6910–6917 (2019).
45. Y. Wu, J. K. Yim, J. Liang, Z. Shao, M. Qi, J. Zhong, Z. Luo, X. Yan, M. Zhang, X. Wang, R. S. Fearing, R. J. Full, L. Lin, Insect-scale fast moving and ultrarobust soft robot. *Sci. Robot.* **4**, eaax1594 (2019).
46. D. Drotman, S. Jadhav, M. Karimi, P. d. Zonia, M. T. Tolley, 3D printed soft actuators for a legged robot capable of navigating unstructured terrain, in *2017 IEEE International Conference on Robotics and Automation (ICRA)* (IEEE, 2017), pp. 5532–5538.
47. N. W. Bartlett, K. P. Becker, R. J. Wood, A fluidic demultiplexer for controlling large arrays of soft actuators. *Soft Matter* **16**, 5871–5877 (2020).
48. M. Trapecar, E. Wogram, D. Svoboda, C. Communal, A. Omer, T. Lungjangwa, P. Sphabmixay, J. Velazquez, K. Schneider, C. W. Wright, S. Mildrum, A. Hendricks, S. Levine, J. Muffat, M. J. Lee, D. A. Lauffenburger, D. Trumper, R. Jaenisch, L. G. Griffith, Human physiomimetic model integrating microphysiological systems of the gut, liver, and brain for studies of neurodegenerative diseases. *Sci. Adv.* **7**, eabd1707 (2021).
49. H. K. Yap, J. H. Lim, F. Nasrallah, C.-H. Yeow, Design and preliminary feasibility study of a soft robotic glove for hand function assistance in stroke survivors. *Front. Neurosci.* **11**, 547 (2017).
50. C. Correia, K. Nuckols, D. Wagner, Y. M. Zhou, M. Clarke, D. Orzel, R. Solinsky, S. Paganoni, C. J. Walsh, Improving grasp function after spinal cord injury with a soft robotic glove. *IEEE Trans. Neural Syst. Rehabil. Eng.* **28**, 1407–1415 (2020).
51. E. W. Hawkes, C. Majidi, M. T. Tolley, Hard questions for soft robotics. *Sci. Robot.* **6**, eabg6049 (2021).
52. K. C. Bhargava, B. Thompson, N. Malmstadt, Discrete elements for 3D microfluidics. *Proc. Natl. Acad. Sci. U.S.A.* **111**, 15013–15018 (2014).
53. A. C. Lamont, A. T. Alsharhan, R. D. Sochol, Geometric determinants of in situ direct laser writing. *Sci. Rep.* **9**, 394 (2019).
54. A. T. Alsharhan, R. Acevedo, R. Warren, R. D. Sochol, 3D microfluidics via cyclic olefin polymer-based *in situ* direct laser writing. *Lab Chip* **19**, 2799–2810 (2019).
55. A. T. Alsharhan, O. M. Young, X. Xu, A. J. Stair, R. D. Sochol, Integrated 3D printed microfluidic circuitry and soft microrobotic actuators via in situ direct laser writing. *J. Micromech. Microeng.* **31**, 044001 (2021).
56. N. Bhattacharjee, C. Parra-Cabrera, Y. T. Kim, A. P. Kuo, A. Folch, Desktop-stereolithography 3D printing of a poly(dimethylsiloxane)-based material with Sylgard-184 properties. *Adv. Mater.* **30**, e1800001 (2018).
57. C. D. Armstrong, N. Todd, A. T. Alsharhan, D. I. Bigio, R. D. Sochol, A 3D-printed morphing nozzle to control fiber orientation during composite additive manufacturing. *Adv. Mater. Technol.* **6**, 2000829 (2021).

Acknowledgments: We greatly appreciate the help and support of A. C. Lamont, M. Restaino, C. Manny, A. Montgomery, C. Simon, E. Hung, N. Cope, S. Merlock, S. Patel, and other members of the Bioinspired Advanced Manufacturing (BAM) Laboratory as well as the technical staff of Terrapin Works including R. Blanton, A. Recklein, C. McCue, F. Aromolaran, and N. Young. **Funding:** This work was supported, in part, by the Center for Engineering Design Concepts and U.S. National Science Foundation (NSF) Award Number 1943356. **Author contributions:** J.D.H., R.A., K.M.E., and R.D.S. conceived the experiments; R.A., J.D.H., and K.M.E. led the experiments with assistance from J.L., K.W., and S.S.; A.T.A. and J.L. led the theoretical simulations with assistance from K.M.E.; J.D.H., R.A., Z.W., K.M.E., and R.D.S. contributed to data analysis and wrote the paper. All authors reviewed the manuscript. **Competing interests:** The authors declare that they have no competing interests. **Data and materials availability:** All data needed to evaluate the conclusions in the paper are present in the paper and/or the Supplementary Materials. Additional data related to this paper may be requested from the authors.

Submitted 27 August 2020
Accepted 3 June 2021
Published 14 July 2021
10.1126/sciadv.abe5257

Citation: J. D. Hubbard, R. Acevedo, K. M. Edwards, A. T. Alsharhan, Z. Wen, J. Landry, K. Wang, S. Schaffer, R. D. Sochol, Fully 3D-printed soft robots with integrated fluidic circuitry. *Sci. Adv.* **7**, eabe5257 (2021).

Science Advances

Fully 3D-printed soft robots with integrated fluidic circuitry

Joshua D. Hubbard, Ruben Acevedo, Kristen M. Edwards, Abdullah T. Alsharhan, Ziteng Wen, Jennifer Landry, Kejin Wang, Saul Schaffer and Ryan D. Sochol

Sci Adv **7** (29), eabe5257.
DOI: 10.1126/sciadv.abe5257